PCCP

ROYAL SOCIETY OF CHEMISTRY

PAPER

View Article Online
View Journal

Cite this: DOI: 10.1039/d5cp01462j

Phase transition and in-plane anisotropy of GeAs under high pressure†

Junbo Wang,[ab] Zilong Zhang,[ab] Shiquan Feng,[ab] Haining Li,[ab] Xiang Zhu,[ab] Kun Yang*[abc] and Xuerui Cheng*[ab]

GeAs exhibits excellent chemical stability and high in-plane anisotropy under ambient conditions. Pressure is one effective approach to regulate structures or properties of two-dimensional materials. In this work, the high-pressure effect on the phase transition and in-plane anisotropic properties is investigated for GeAs using Raman spectroscopy, infrared spectroscopy, high-pressure resistance measurement, and density functional theory calculations. The results show that GeAs undergoes an irreversible monoclinic-to-cubic transition around 18.4 GPa during compression. IR and resistivity measurements indicate that this cubic rock-salt structure exhibits a metallic state. Upon decompression, high-pressure cubic GeAs converts to a tetragonal structure rather than the initial monoclinic structure. Moreover, tetragonal GeAs also exhibits a metallic state. This transition is reversible, as tetragonal GeAs will convert back to cubic GeAs around 18.2 GPa. Angle-resolved polarized Raman spectroscopy reveals that for both A_g and B_g modes of monoclinic GeAs, pressure will induce a 10°–15° deflection in their polarization direction up to 10 GPa, but has no effect on their anisotropy periods. Tetragonal GeAs also exhibits excellent in-plane optical anisotropy with a period of 180°. But different from monoclinic GeAs, both the polarization direction and periods remain stable in its Raman mode under pressure. The result is conducive to understanding the structural stability and anisotropic properties of GeAs.

Received 16th April 2025,
Accepted 22nd July 2025

DOI: 10.1039/d5cp01462j

rsc.li/pccp

Introduction

Two-dimensional (2D) layered materials have received increasing attention in recent years due to their unique physical properties. Many types of novel 2D materials have been studied, including graphene, 2D transition metal dichalcogenides (TMDs), black phosphorus (BP), and silicene.[1–8] Recently, IV–V group compounds, as one new class of 2D materials, have become a research hotspot. There are two crystal structures for IV–V group compounds: the orthorhombic structure (such as SiP, SiP_2, and $GeAs_2$) and the monoclinic structure (such as GeP, GeAs, and SiAs).[9–16] Among them, GeAs belongs to the monoclinic structure with a space group of *C*2/*m*. For this layered structure, each Ge atom is coordinated by one Ge atom and three As atoms, while each As atom is connected to three Ge atoms in the *a*–*b* plane layer. Adjacent layers are stacked along the *c*-axis through van der Waals forces.

GeAs is one semiconductor material with a narrow bandgap (~1.4 eV) and exhibits excellent chemical stability, high carrier mobility and broad-band absorption. Especially, GeAs exhibits high in-plane anisotropy (anisotropic mobility ratio of 4.8).[10] Kim *et al.* demonstrated that a multilayer GeAs transistor exhibits p-type transport characteristics, featuring a low flat band Schottky barrier height of 21.7 meV at room temperature.[17] Few-layer GeAs field-effect transistors (FETs) have been reported to possess a carrier mobility up to 100 $cm^2 V^{-1} s^{-1}$, and their ON–OFF ratio is over 10^5.[10] Due to its excellent anisotropy, GeAs has promising applications in polarized photodetectors and polarized optical imaging. However, its dark current is high, leading to a relatively low specific detection ratio and small dichroic ratio, which limits its application.[18]

To further improve its properties and expand its application, several strategies have been introduced, such as heterojunction formation and strain engineering. The GeAs/InSe heterojunction exhibits a low dark current of about 0.1 pA, a high photoresponsivity of 357 mA W^{-1}, and a photo-switching ratio of 10^3, exhibiting a favorable photovoltaic effect.[19] Besides the heterojunction, pressure as one type of strain has also been extensively used to tune the structure and properties of 2D materials.[20,21] Pressure-induced phase transitions, metallization, and even superconductivity have been observed for 2D materials. For example, BP changes from the orthorhombic to rhombohedral

[a] College of Electronics and Information, Zhengzhou University of Light Industry, Zhengzhou, Henan, P. R. China. E-mail: yyyk2002@163.com, xrcheng@zzuli.edu.cn
[b] Henan key Laboratory of Magnetoelectric Information Functional Materials, Zhengzhou, Henan, P. R. China
[c] School of Physics and Optoelectronic Engineering, Zhongyuan University of Technology, Zhengzhou, Henan, P. R. China

† Electronic supplementary information (ESI) available. See DOI: https://doi.org/10.1039/d5cp01462j

structure with a semiconductor-to-semimetal transition at 4.5 GPa and then exhibits metallic and superconducting states at 10 GPa and 32 GPa, respectively.[22,23] Similar pressure-induced phase transition has also been observed for MoS_2.[24–26] Besides structure transition, pressure can also effectively tune the anisotropy for 2D materials. It has been reported that the polarized direction varies with pressure for 2D InSe, which is shifted by 15° when the pressure reaches 3.3 GPa.[27] For $ReSe_2$, the polarized direction experiences a rotation of 55°, and the polarization period changes from 180° to 90° at 7.5 GPa for the A_g mode (174 cm^{-1}).[28] Moreover, the conductance and mobility of the few-layer $ReSe_2$ FET increase with decreasing pressure.[29] Therefore, abundant structural and performance variations have been observed under pressure for 2D materials.

It has been reported that GeAs would undergo a monoclinic to cubic rock-salt ($Fm\bar{3}m$) phase transition around 10 GPa during compression. More interestingly, this is an irreversible transition, and this high-pressure rock-salt phase will convert back to a new tetragonal structure ($I4mm$) rather than the initial monoclinic structure upon decompression.[30] Moreover, this high-pressure rock salt GeAs is reported to be one metallic phase, even exhibiting superconductivity characteristics.[31] In contrast, research on the new tetragonal GeAs, obtained during the decompression process, is rarely reported. Whether it is one semiconductor or metal is still unclear for this tetragonal structure. In addition, monoclinic GeAs is known to be an anisotropic semiconductor, while whether tetragonal GeAs possesses polarization characteristics remains unreported. Moreover, although this new structure is obtained under high-pressure conditions, its structural stability under high pressure is still unknown. Besides phase transition, the pressure effect on the anisotropic properties of GeAs is rarely reported. Therefore, further research is necessary for GeAs, especially for this new tetragonal structure.

In this work, high-pressure Raman spectroscopy was used to study the phase transition for bulk GeAs, especially the structural stability of tetragonal GeAs. High-pressure electrical measurements and infrared spectroscopy were used to explore the metallic or semiconductor characteristics for different types of GeAs structures. The pressure effect on the in-plane optical anisotropy of GeAs was investigated using polarization angle-resolved Raman spectroscopy.

2. Experimental

GeAs with a thickness of 40–70 nm was mechanically exfoliated from a bulk GeAs crystal purchased from Nanjing Muke Nano Technology Co., Ltd (Nanjing China). High-pressure experiments were performed using a 300 μm diamond anvil cell (DAC). The sample chamber is a 100 μm-diameter hole drilled in a metal gasket (T301). High-pressure Raman and polarization angle-resolved Raman spectra were measured using a Renishaw Raman microscope (United Kingdom) equipped with a 532 nm laser system. High-pressure infrared spectroscopy was conducted using a Fourier-transform spectrometer (Bruker 70 v) equipped with an infrared microscope (Hyperion 2000) using a type IIa DAC. Silicon oil and KBr were used as pressure transmitting media (PTM) for Raman and IR measurements, respectively, which can maintain the hydrostatic pressure up to 4 GPa.[32] High-pressure resistivity was measured in a DAC using four-probe electrical measurements. Cubic boron nitride (c-BN) was used to insulate the metallic T301 gasket. Four thin platinum layers were used as the electrical probes. KBr powder was used as the pressure-transmitting medium. The electrical resistivity was measured using a Keithley 6221 current source and a 2182A nanovoltmeter. The pressure was calibrated by fluorescence displacement of ruby at room temperature using Raman spectroscopy with a resolution of 1 cm^{-1} and a pressure accuracy of about 0.2 GPa.[33]

The schematic diagram of two configurations (parallel and cross) for angle-resolved polarized Raman spectroscopy is shown in Fig. S1 of the ESI.† Polarization angle-resolved Raman spectroscopy measurements are achieved by adding a polarizer in the incident light path. The polarization direction of the scattered light path is parallel to the polarization direction of the incident light for the parallel configuration and perpendicular to the polarization direction of the incident light for the cross configuration. In this study, the symbol "$\parallel$" is used to denote the parallel configuration, and the symbol "$\perp$" is used to denote the cross configuration.[34] To avoid the laser heating effect, the incident laser power was fixed to 1 mW during the experiment.

The band structure and formation enthalpy were calculated using first-principles methods with the VASP code, employing the generalized gradient approximation (GGA) with the Perdew–Burke–Ernzerhof (PBE) parameter as the exchange–correlation potential functional.[35,36] The calculations were done with a plane-wave cutoff energy of 520 eV and a k-point mesh of 13 × 13 × 12. The lattice parameters and atomic positions were optimized until the total energy converged to less than 1×10^{-6} eV per atom and the atomic forces were less than 0.01 eV $Å^{-1}$. Phonon calculations were carried out using density functional perturbation theory (DFPT) as implemented in the Quantum ESPRESSO package, employing an 8 × 8 × 8 q-point mesh to sample the phonon Brillouin zone.[37,38] The theoretically calculated lattice parameters for all three GeAs phases (monoclinic, rock-salt, and tetragonal) are given in Table S1 (ESI†).

3. Results and discussion

High-pressure Raman spectroscopy was carried out to study the phase transition of GeAs under pressure, as shown in Fig. 1. Its theoretical Raman spectra were calculated using the first-principles calculations to help identify its Raman peak, as shown in Fig. S2 (ESI†). The calculated results are consistent with the experimental results. At ambient pressure, 11 Raman-active modes can be observed for GeAs in the experiment. Among them, Raman peaks located at 91, 103, 145, 172, 273, 282, and 306 cm^{-1} correspond to the A_g modes, while the Raman modes at 73, 84, 242, and 256 cm^{-1} belong to the B_g modes. Upon applying pressure, all Raman peaks shift to

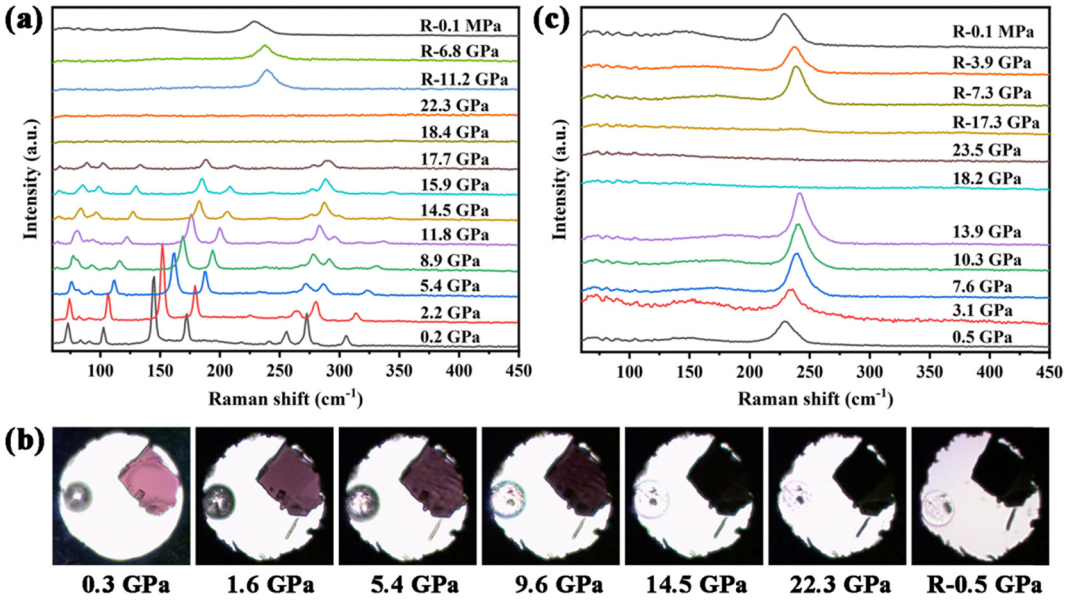

Fig. 1 The evolution of Raman spectra of bulk GeAs in the (a) first and (c) second pressure up-down cycles. (b) Optical photographs of GeAs under several pressures in the first cycle.

higher frequencies, accompanied by the width broadening and intensity reduction. It is noteworthy that all Raman peaks suddenly disappear when the pressure reaches 18.4 GPa. And further increasing pressure to 22.3 GPa, all Raman peaks remain invisible. This result is similar to the phenomenon observed by Liu *et al.*, which was attributed to the monoclinic-to-cubic rock-salt structure phase transition.[31] During the decompression process, when the pressure decreases to 11.2 GPa, a new broad peak appears around 240 cm^{-1}, which was not observed in the compression process. This new peak exhibits a redshift as the pressure decreases and remains visible after releasing to atmospheric pressure. This peak has been attributed to the characteristic peak of tetragonal GeAs. Therefore, it can be determined that GeAs transforms from the HP rock-salt structure to the tetragonal structure during decompression. Accompanied by the above phase transition, its optical photographs also vary with pressure, as shown in Fig. 1. It can be seen that the initial monoclinic GeAs is semi-transparent at ambient pressure. However, above 10 GPa, the sample transforms into a black opaque state because of the monoclinic-to-cubic phase transition. Moreover, GeAs remains in the black opaque state during the decompression.

Although the structure presented during decompression has been identified to be the tetragonal phase for GeAs, whether it is stable under high pressure is not yet known. To investigate its stability, a high-pressure study was performed on the above tetragonal GeAs, as shown in Fig. 1. When the pressure increases to 18.2 GPa, all Raman modes disappear again, which is similar to the above result of monoclinic GeAs observed at 18.4 GPa. While releasing pressure, the initial characteristic peak of the tetragonal GeAs appears again. Consequently, it can be assumed that similar to the monoclinic structure, tetragonal GeAs is also unstable under pressure, which will convert to the HP rock-salt structure around 18.2 GPa.

High-pressure resistance measurements were performed to investigate the electrical properties of different types of GeAs structures. As shown in Fig. 2, its resistivity continuously decreases upon compression. Up to 10.2 GPa, its resistivity decreases from 92 to 22.7 mΩ cm, approximately a four-fold decrease. Subsequently, in the range of 10.2–19.4 GPa, its resistivity decreases rapidly from 22.7 to 0.15 mΩ cm, a 147-fold decrease, which is attributed to the transition from the monoclinic phase to the rock-salt phase, while above 19.4 GPa, its resistivity almost stabilizes, indicating that the initial monoclinic GeAs completely transforms into the HP rock salt structure, consistent with the above Raman results. It is interesting that although there is a cubic-to-tetragonal phase transition during decompression, its resistivity almost remains unchanged during pressure release.

To further judge whether it is a semiconductor or metal state, temperature-dependent resistivity has been measured within the temperature range of 25–80 °C at different pressures. It can be observed in Fig. 2 that at 10.2 GPa, its electrical resistivity decreases with increasing temperature, indicating a semiconducting state due to thermally activated charge carriers. In contrast, at 10.2 GPa and 16.3 GPa, its resistivity increases with temperature in the low-temperature region, remaining almost constant in the high-temperature region. Above 19.4 GPa, its resistivity increases over the entire temperature range, exhibiting metallic properties. Therefore, the monoclinic-to-rock salt phase transition around 19 GPa can be attributed to a semiconductor-to-metal transition. Combining with the above Raman results, it can be confirmed that this transition first occurs at 10.2 GPa and completely finishes around 19 GPa, while both structures coexist within the above pressure range, as shown in Fig. 2. The coexistence of semiconducting and metallic states may be caused by non-hydrostatic effects. Resistivity measurements as a function of temperature have also been conducted for tetragonal GeAs during decompression, as shown in Fig. 2.

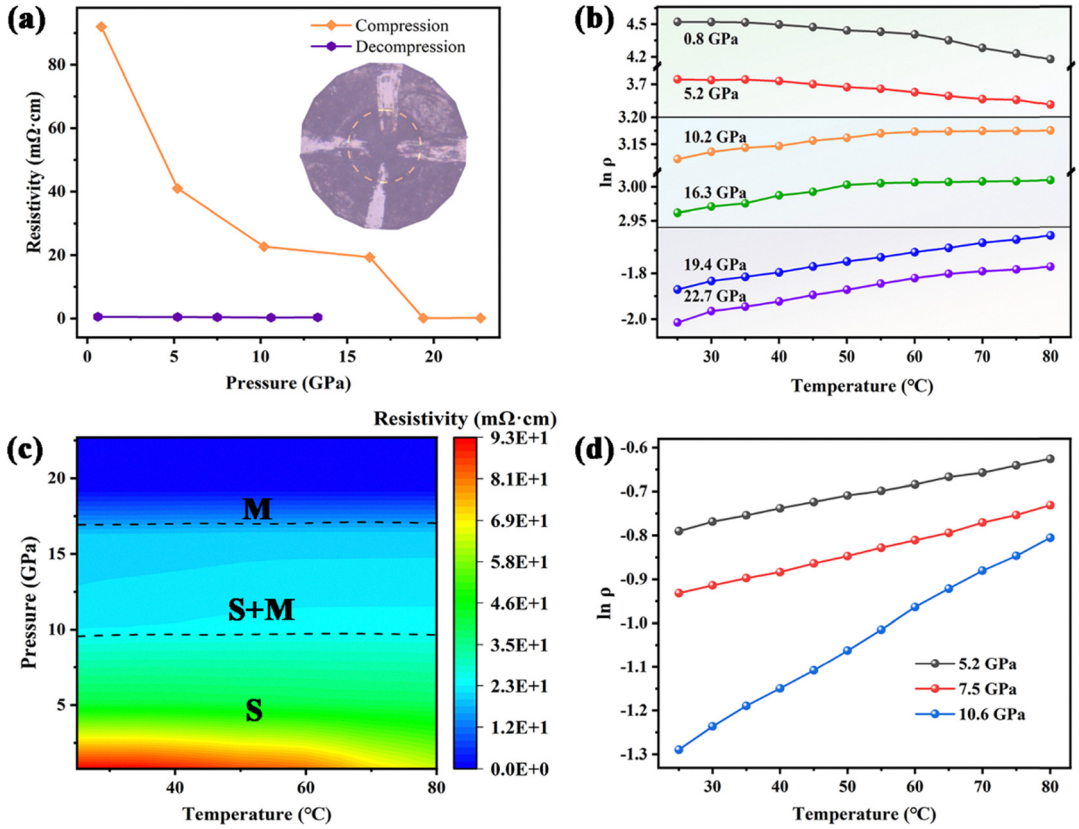

Fig. 2 (a) Variation of resistivity of GeAs with pressure. (b) Pressure-dependent resistivity of GeAs in the temperature range of 25–80 °C. (c) Temperature–pressure resistivity contour map. (d) Temperature dependence of resistivity of the tetragonal phase GeAs at different pressures.

Evidently, the tetragonal GeAs exhibits low resistivity, and its resistivity increases with temperature rise. Therefore, it can be confirmed that tetragonal GeAs is one metallic state.

Besides resistivity measurements, infrared spectroscopy is also an effective method for characterizing pressure-induced metallization. Fig. 3 displays the infrared reflectance spectrum of GeAs under high pressure, in which the weak reflectance within the range of 1800–2600 cm^{-1} is due to the absorption of the diamond. It can be observed that below 11.4 GPa, its reflectance increases slowly with increasing pressure. However, above 11.4 GPa, its reflectance rapidly increases until 18.3 GPa. Simultaneously, a rapid decrease can also be observed in its transmission spectrum between 11.4 GPa and 18.3 GPa, as shown in Fig. S3 (ESI†). Counts of the ADC (analog-to-digital converter) exhibit a clearer variation in its reflectivity and transmittance, as plotted in the inset. The increase of reflectance implies a metal state above 18.3 GPa for GeAs. Therefore, three different states are present with increasing pressure for GeAs: the semiconductor state below 11.4 GPa, the metal state above 18.3 GPa, and the mixture of both states in the intermediate pressure range of 11.4–18.3 GPa. This result agrees well with the above high-pressure Raman and resistivity results.

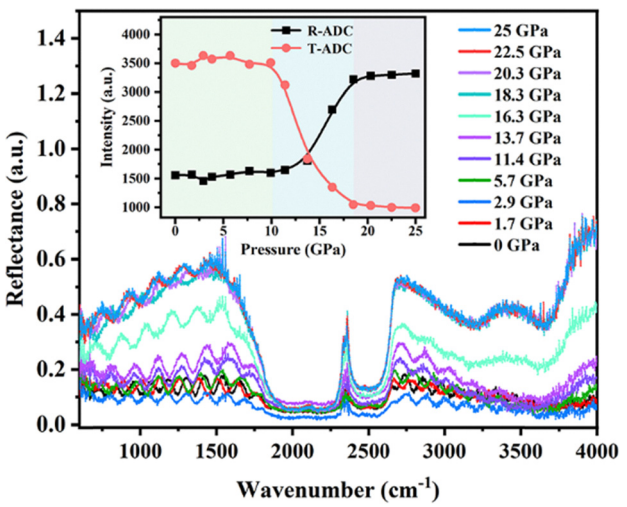

Fig. 3 Representative pressure-dependent infrared reflectance spectra of GeAs. The inset shows the variation of ADC counts of reflectance and transmittance with pressure.

The energy band structure of GeAs is determined to explain the above semiconductor-to-metal transition. As shown in Fig. 4, at atmospheric pressure, GeAs is an indirect band structure with a gap of 0.56 eV, slightly below the previous result of 0.65 eV.[39] This is because the GGA-PBE method tends to underestimate the absolute value of the band-gap energy, but it still gives an accurate description of its change with pressure.[40] As can be clearly discerned, the energy of its conduction band minimum (CBM) first decreases and then increases

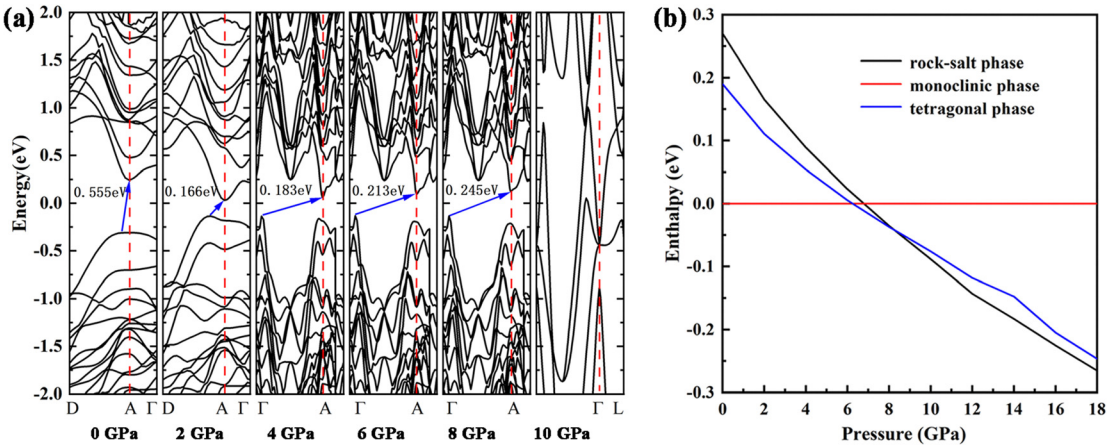

Fig. 4 (a) The DFT-calculated band structure of GeAs at high pressures. (b) Calculated formation enthalpy as a function of pressure for the GeAs unit cell.

with rising pressure, while the valence band maximum (VBM) almost remains unchanged, leading to an initial decrease followed by an increase for its band gap. When the pressure is increased to 10 GPa, its valence band crosses the conduction band, indicating one metallic state. The band structure of the tetragonal phase under ambient conditions has also been determined, as shown in Fig. S4 (ESI†). Its valence band crosses the conduction band, indicating that tetragonal GeAs is also one metallic state, in agreement with the above electrical results.

First-principles calculations further confirm that superconductivity emerges for the HP rock-salt phase and tetragonal phase. The phonon dispersion curves and the Eliashberg spectral function $\alpha^2F(\omega)$ for both the cubic and tetragonal phases of GeAs are presented in Fig. S5 (ESI†). For the high-pressure cubic phase (16 GPa), the electron–phonon coupling constant is λ = 0.61 and the logarithmic average phonon frequency is $\omega_{\log}$ = 211.3 K, yielding a superconducting transition temperature of T_c = 5.1 K. In comparison, the ambient-pressure tetragonal phase exhibits λ = 0.58 and $\omega_{\log}$ = 157.5 K, corresponding to a lower T_c of 3.18 K. These results are obtained using McMillan's equation with a Coulomb pseudopotential μ^* = 0.10.[41,42] These values agree well with previous reports and indicate that pressure enhances the superconducting properties of GeAs by favoring the cubic phase with stronger electron–phonon interactions and higher phonon frequencies.[31] The pressure dependence of lattice parameters and volume *versus* pressure is also calculated for three different types of GeAs structures, as shown in Fig. S6 (ESI†). The unit-cell volume *versus* pressure are fitted using a third-order Birch–Murnaghan equation of state (EOS) (eqn (1)):

$$P = 1.5B_0\left[\left(\frac{V}{V_0}\right)^{-\frac{7}{3}} - \left(\frac{V}{V_0}\right)^{-\frac{5}{3}}\right]\left\{1 - 0.75\left(4 - B_0'\right)\left[\left(\frac{V}{V_0}\right)^{-\frac{2}{3}} - 1\right]\right\} \quad (1)$$

where B_0 and V_0 represent the bulk modulus and the unit-cell volume under ambient conditions, respectively, and B_0' is the pressure derivative. As shown in Fig. S6 (ESI†), the obtained values of bulk modulus B_0 are 24.7, 76.3 and 68.2 GPa for monoclinic, cubic and tetragonal GeAs, respectively. It can be observed that monoclinic GeAs has the smallest value, making this structure easy to compress.

Additionally, the formation enthalpy of three different structures of GeAs was calculated under pressure, as plotted in Fig. 4, in which the enthalpy of the monoclinic phase serves as the reference zero point. Lower enthalpy indicates higher thermodynamic stability. Hence, the monoclinic phase is the most stable structure for GeAs at ambient pressure. Once the pressure exceeds 8 GPa, the rock-salt phase possesses the lowest enthalpy. Therefore, GeAs will exist in the rock-salt structure above 8 GPa. It is interesting to note that in the middle pressure range of 6–8 GPa, the enthalpy of the tetragonal structure is lower than that of the rock-salt phase. But the enthalpy difference between the two structures is so small and the pressure range is so narrow that the tetragonal structure was not detected in the experiment during compression. Thus, this tetragonal structure is observed during the decompression process. Therefore, the theoretical calculation is consistent with the above high-pressure Raman results, further affirming the pressure-induced structural evolution of GeAs.

Monoclinic GeAs exhibits excellent anisotropy under ambient conditions. However, the variation of its polarization characteristics under high pressure remains unknown. Especially, the anisotropy properties of the new structure of tetragonal GeAs are still unclear. Therefore, polarization angle-resolved Raman spectroscopy was *in situ* carried out under pressure for GeAs. As shown in Fig. S7 (ESI†), Raman intensities exhibit periodic variation for monoclinic GeAs. To clearly exhibit the correlation between Raman intensity and polarization angle, the polar plots of Raman intensity *versus* angle were fitted using the formula in the study by Yang *et al.*,[43] as shown in Fig. S8 (ESI†). For the parallel configuration, the Raman intensity of the A_g mode is defined as eqn (2)

$$I^{\mathrm{Para}}(\mathrm{A_g}) \propto \left[\cos^2(\theta) + \frac{a}{b}\cdot\sin^2(\theta)\cdot\cos\varnothing_{ab}\right]^2 + \sin^2(\theta)\sin^2(\varnothing_{ab}) \quad (2)$$

and for B_g mode, the intensity is defined as in eqn (3)

$$I^{\mathrm{Para}}(\mathrm{B_g}) \propto 4|e|^2\sin^2(\theta)\cos^2(\theta) \quad (3)$$

while for the cross configuration, the Raman intensity of the A_g mode is defined as in eqn (4)

$$I^{\mathrm{Cross}}(\mathrm{A_g}) \propto \left\{\left[\cos(\varnothing_{ab}) - \frac{a}{b}\right]^2 + \sin^2(\varnothing_{ab})\right\} \sin^2(\theta)\cos^2(\theta) \quad (4)$$

and for the B_g mode, the intensity is defined as in eqn (5)

$$I^{\mathrm{Cross}}(\mathrm{B_g}) \propto e^2 \cos^2(2\theta) \quad (5)$$

In the above definition, θ represents the angle between the incident light and the crystal axis a, while ϕ_{ab} denotes the phase difference between the Raman tensors a and b. In the parallel configuration, the intensities of A_g modes at 145 and 173 cm^{-1} reach maxima at 0° and 180°, while showing minima at 90° and 270°, whereas the maximum intensities of the A_g modes located at 91 and 282 cm^{-1} appear at about 120°. Therefore, for different A_g modes, the maximum intensity occurs at different polarization angles, but they share the same period of 180°, exhibiting a spindle-like shape. Interestingly, A_g modes located at 91 and 282 cm^{-1} exhibit noticeable sub-maxima in both configurations. This result is similar to the phenomenon observed by Yang *et al.*[43] Different from A_g modes, the polar plot of B_g modes at 73 and 256 cm^{-1} exhibit a four-leaf clover shape in both configurations, with an approximate 45° rotation and a period of 90°. The differences in the Raman intensity are attributed to its varying response to linearly polarized light along different directions.[18,44]

Fig. 5 shows the polarization angle-resolved Raman intensity of monoclinic GeAs at different pressures. It can be seen that the anisotropy period of both A_g and B_g modes remains unchanged, but its polarization direction shows variation as the pressure increases. When the pressure reaches 10 GPa, the polarization directions of the A_g and B_g modes exhibit rotations of 10° and 15°, respectively. Besides monoclinic GeAs, the Raman intensity of tetragonal GeAs also exhibits a periodic variation with the polarization angle, as shown in Fig. S9 (ESI†). The pressure-dependent polar plot for the tetragonal GeAs is also plotted, as shown in Fig. 6. The Raman intensity shows a maximum at 0° for the parallel configuration and at 90° for the cross configuration. Both configurations exhibit the same periodic variation of 180°, accompanied by slight pressure-induced rotations of their polarization directions.

4. Conclusions

In summary, we investigate the structural evolution of GeAs under pressure. The results show that monoclinic GeAs is unstable under high pressure, and will undergo a phase transition at 18.4 GPa. This HP phase adopts a cubic rock-salt structure and exhibits a metallic state. Moreover, this phase transition is irreversible, as the HP cubic phase will convert to a tetragonal structure rather than the initial monoclinic structure at 7.7 GPa during compression. Resistivity measurement results indicate that this tetragonal GeAs also exhibits metallization. Furthermore, tetragonal GeAs is also unstable under pressure, which will convert back to the cubic rock-salt structure at 18.2 GPa. Angle-resolved polarization Raman spectroscopy shows that both monoclinic and tetragonal GeAs

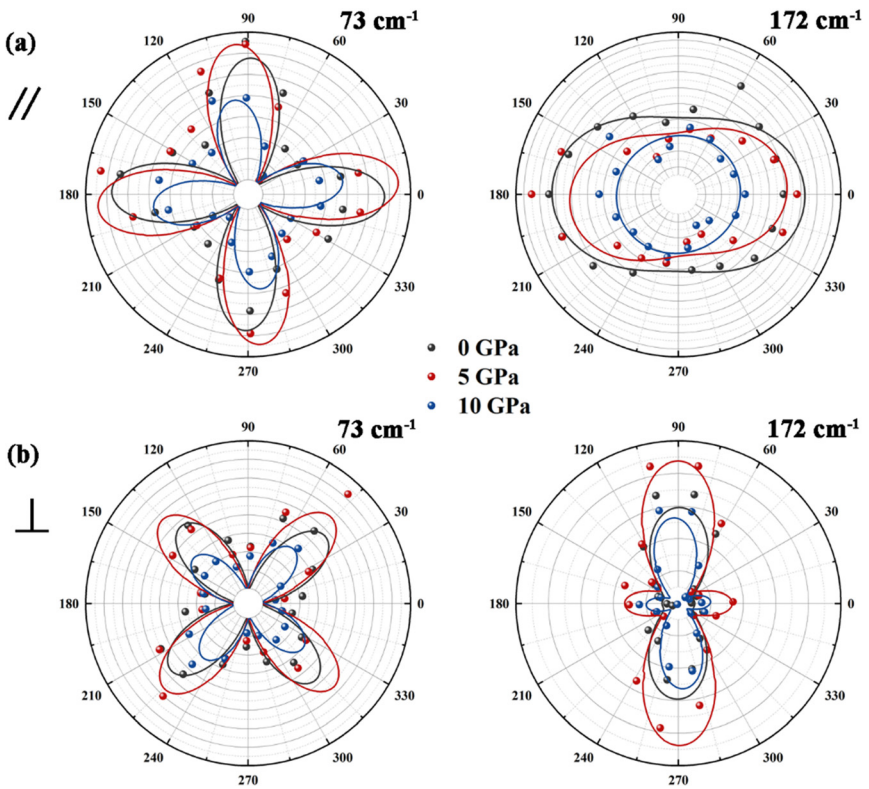

Fig. 5 Polarization diagrams of the intensity of the 73 cm^{-1} (B_g) and 172 cm^{-1} (A_g) Raman mode in (a) parallel and (b) cross configurations.

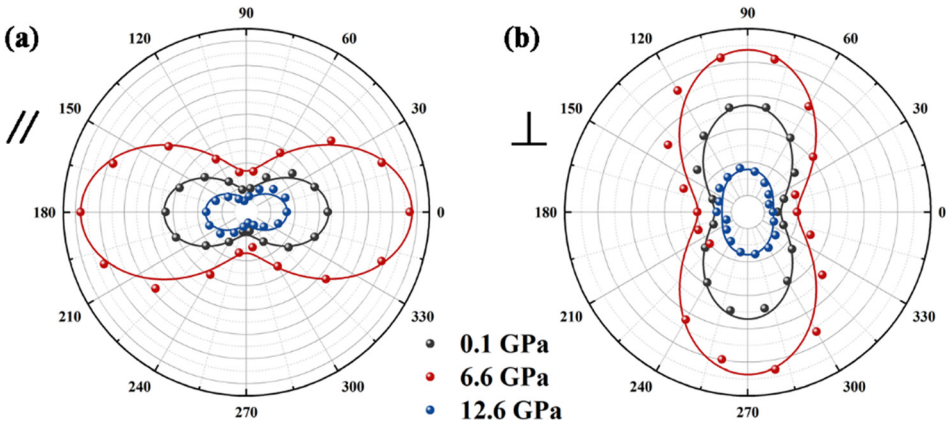

Fig. 6 The pressure-dependent Raman intensity polar plots of the tetragonal GeAs.

exhibit excellent in-plane optical anisotropy. For monoclinic GeAs, most A_g Raman modes possess a polarization period of 180°, while B_g modes have a polarization period of 90°. During compression, pressure does not change the polarization periods for both A_g and B_g modes, but the pressure will affect their polarization direction. At 10 GPa, the polarization directions of the A_g and B_g modes exhibit a 10–15° rotation. Furthermore, it was observed that the Raman intensity of tetragonal GeAs exhibits a 180° periodic variation with polarization angle, further confirming its optical anisotropy. Within a certain pressure range, both monoclinic and tetragonal phases of GeAs maintain significant in-plane optical anisotropy, and pressure has a certain tuning effect on its optical anisotropy.

Conflicts of interest

There are no conflicts to declare.

Data availability

All relevant data are within the manuscript and its ESI.†

Acknowledgements

This work was supported by the National Science Foundation of China (no. 12104415) and the Key Research Project of Department of Science and Technology in Henan Province (no. 252102210192). Project of Anhui Province Key Laboratory of Pollutant Sensitive Materials and Environmental Remediation (no. PSMER2023007).

References

1 X. Wang, Y. Cui, T. Li, M. Lei, J. Li and Z. Wei, *Adv. Opt. Mater.*, 2019, **7**, 1801274.
2 Z. Lou, Z. Liang and G. Shen, *J. Semicond.*, 2016, **37**, 091001.
3 M. Amani, E. Regan, J. Bullock, G. H. Ahn and A. Javey, *ACS Nano*, 2017, **11**, 11724–11731.
4 T. Hong, B. Chamlagain, W. Lin, H.-J. Chuang, M. Pan, Z. Zhou and Y.-Q. Xu, *Nanoscale*, 2014, **6**, 8978–8983.
5 Y. Li, Y. Wang, L. Huang, X. Wang, X. Li, H.-X. Deng, Z. Wei and J. Li, *ACS Appl. Mater. Interfaces*, 2016, **8**, 15574–15581.
6 H. Oughaddou, H. Enriquez, M. R. Tchalala, H. Yildirim, A. J. Mayne, A. Bendounan, G. Dujardin, M. Ait Ali and A. Kara, *Prog. Surf. Sci.*, 2015, **90**, 46–83.
7 P. Bora, S. Kumar and D. Sinha, *Mater. Today Sustainability*, 2024, **27**, 100914.
8 S. A. Ali, B. Ahmed, A. Javed, M. U. Muzaffar, A. Bano and A. Ulhaq, *Appl. Phys. Lett.*, 2024, **125**, 231902.
9 C. Barreteau, B. Michon, C. Besnard and E. Giannini, *J. Cryst. Growth*, 2016, **443**, 75–80.
10 J. Guo, Y. Liu, Y. Ma, E. Zhu, S. Lee, Z. Lu, Z. Zhao, C. Xu, S.-J. Lee, H. Wu, K. Kovnir, Y. Huang and X. Duan, *Adv. Mater.*, 2018, **30**, 1705934.
11 L. Li, P. Gong, D. Sheng, S. Wang, W. Wang, X. Zhu, X. Shi, F. Wang, W. Han, S. Yang, K. Liu, H. Li and T. Zhai, *Adv. Mater.*, 2018, **30**, 1804541.
12 L. Li, W. Wang, P. Gong, X. Zhu, B. Deng, X. Shi, G. Gao, H. Li and T. Zhai, *Adv. Mater.*, 2018, **30**, 1706771.
13 Z. Wang, J. Guo, Y. Zhang, J. Liu, J. S. Ponraj, S. C. Dhanabalan, T. Zhai, X. Liu, Y. Song and H. Zhang, *Nanophotonics*, 2020, **9**, 3645–3654.
14 B. Mortazavi and T. Rabczuk, *Phys. E*, 2018, **103**, 273–278.
15 C. Li, S. Wang, C. Li, T. Yu, N. Jia, J. Qiao, M. Zhu, D. Liu and X. Tao, *J. Mater. Chem. C*, 2018, **6**, 7219–7225.
16 Y. Suzuki, N. Urakami and Y. Hashimoto, *Mater. Lett.*, 2021, **283**, 128748.
17 J. H. Kim, G. H. Han and B. H. Moon, *Nanotechnology*, 2023, **34**, 315201.
18 Z. Zhou, M. Long, L. Pan, X. Wang, M. Zhong, M. Blei, J. Wang, J. Fang, S. Tongay, W. Hu, J. Li and Z. Wei, *ACS Nano*, 2018, **12**, 12416–12423.
19 J. Xiong, Y. Sun, L. Wu, W. Wang, W. Gao, N. Huo and J. Li, *Adv. Opt. Mater.*, 2021, **9**, 2101017.
20 M. Mączka, S. Sobczak, P. Ratajczyk, F. F. Leite, W. Paraguassu, F. Dybała, A. P. Herman, R. Kudrawiec and A. Katrusiak, *Chem. Mater.*, 2022, **34**, 7867–7877.

21 S. Conejeros, P. Alemany and E. Canadell, *Phys. Rev. B*, 2023, **108**, 214109.
22 S. N. Gupta, A. Singh, K. Pal, B. Chakraborti, D. V. S. Muthu, U. V. Waghmare and A. K. Sood, *Phys. Rev. B*, 2017, **96**, 094104.
23 M. Karuzawa, M. Ishizuka and S. Endo, *J. Phys.: Condens. Matter*, 2002, **14**, 10759.
24 Y. Zhuang, L. Dai, L. Wu, H. Li, H. Hu, K. Liu, L. Yang and C. Pu, *Appl. Phys. Lett.*, 2017, **110**, 122103.
25 Z. Zhao, H. Zhang, H. Yuan, S. Wang, Y. Lin, Q. Zeng, G. Xu, Z. Liu, G. K. Solanki, K. D. Patel, Y. Cui, H. Y. Hwang and W. L. Mao, *Nat. Commun.*, 2015, **6**, 7312.
26 A. P. Nayak, S. Bhattacharyya, J. Zhu, J. Liu, X. Wu, T. Pandey, C. Jin, A. K. Singh, D. Akinwande and J.-F. Lin, *Nat. Commun.*, 2014, **5**, 3731.
27 X. Cheng, Z. Huangfu, J. Wang, H. Zhang, S. Feng, Y. Liang, X. Zhu, Z. Wang, X. Wu and K. Yang, *J. Alloys Compd.*, 2024, **970**, 172636.
28 Y. Yan, L. Chen, K. Dai, Y. Li, L. Wang, K. Jiang, A. Cui, J. Zhang and Z. Hu, *J. Phys. Chem. Lett.*, 2023, **14**, 7618–7625.
29 K. Intonti, E. Faella, L. Viscardi, A. Kumar, O. Durante, F. Giubileo, M. Passacantando, H. T. Lam, K. Anastasiou, M. F. Craciun, S. Russo and A. Di Bartolomeo, *Adv. Electron. Mater.*, 2023, **9**, 2300066.
30 U. Schwarz and K. Syassen, *High Pressure Res.*, 1992, **9**, 148–152.
31 L. Liu, V. V. Struzhkin and J. Ying, *Phys. Rev. B*, 2019, **100**, 214516.
32 D. Errandonea, Y. Meng, M. Somayazulu and D. Häusermann, *Phys. B*, 2005, **355**, 116–125.
33 H. K. Mao, J. Xu and P. M. Bell, *J. Geophys. Res.: Solid Earth*, 1986, **91**, 4673–4676.
34 X.-L. Liu, X. Zhang, M.-L. Lin and P.-H. Tan, *Chin. Phys. B*, 2017, **26**, 067802.
35 G. Kresse and J. Furthmüller, *Phys. Rev. B: Condens. Matter Mater. Phys.*, 1996, **54**, 11169–11186.
36 G. Kresse and D. Joubert, *Phys. Rev. B: Condens. Matter Mater. Phys.*, 1999, **59**, 1758–1775.
37 S. Baroni, S. de Gironcoli, A. Dal Corso and P. Giannozzi, *Rev. Mod. Phys.*, 2001, **73**, 515–562.
38 P. Giannozzi, S. Baroni, N. Bonini, M. Calandra, R. Car, C. Cavazzoni, D. Ceresoli, G. L. Chiarotti, M. Cococcioni, I. Dabo, A. Dal Corso, S. de Gironcoli, S. Fabris, G. Fratesi, R. Gebauer, U. Gerstmann, C. Gougoussis, A. Kokalj, M. Lazzeri, L. Martin-Samos, N. Marzari, F. Mauri, R. Mazzarello, S. Paolini, A. Pasquarello, L. Paulatto, C. Sbraccia, S. Scandolo, G. Sclauzero, A. P. Seitsonen, A. Smogunov, P. Umari and R. M. Wentzcovitch, *J. Phys.: Condens. Matter*, 2009, **21**, 395502.
39 J. W. Rau and C. R. Kannewurf, *Phys. Rev. B: Condens. Matter Mater. Phys.*, 1971, **3**, 2581–2587.
40 T. Ouahrani, R. M. Boufatah, M. Benaissa, Á. Morales-García, M. Badawi and D. Errandonea, *Phys. Rev. Mater.*, 2023, **7**, 025403.
41 W. L. McMillan, *Phys. Rev.*, 1968, **167**, 331–344.
42 P. B. Allen and R. C. Dynes, *Phys. Rev. B: Condens. Matter Mater. Phys.*, 1975, **12**, 905–922.
43 S. Yang, Y. Yang, M. Wu, C. Hu, W. Shen, Y. Gong, L. Huang, C. Jiang, Y. Zhang and P. M. Ajayan, *Adv. Funct. Mater.*, 2018, **28**, 1707379.
44 H. Sar, J. Gao and X. Yang, *Sci. Rep.*, 2020, **10**, 14282.

